Chemical Science

ROYAL SOCIETY OF CHEMISTRY

EDGE ARTICLE

View Article Online
View Journal | View Issue

Cite this: *Chem. Sci.*, 2026, **17**, 2340

All publication charges for this article have been paid for by the Royal Society of Chemistry

A pyridinium cation engineering strategy to achieve high-performance X-ray scintillation of antimony halides

Yuan-Yuan Zhao,[ab] Jian-Cheng Chen,[ab] Li Zhang,[c] Jiabin Chen,*[c] Qing Liao,*[d] Zhong-Qiu Li,*[ac] Meijin Lin,[cd] Jiannian Yao[abc] and Yu-Wu Zhong*[ac]

While organic–inorganic hybrid metal halides (OIMHs) have emerged as promising X-ray scintillators, a major challenge lies in the precise control of their structural dimensionality and exciton behavior to optimize the scintillation performance. Here, we introduce a pyridinium cation engineering strategy to address this issue. A one-pot reaction of $SbCl_3$ with a pyridine derivative, in the presence of HCl, yields either a 0D or 1D Sb-based OIMH. The 0D structure featuring isolated $[SbCl_5]^{2-}$ polyhedra imposes strong quantum confinement, leading to enhanced electron-phonon coupling. This results in an orange-red self-trapped exciton emission at 630 nm, characterized by a large Stokes shift of 262 nm and a near-unity photoluminescence quantum yield. This 0D material demonstrates high-performance X-ray scintillation with a light yield of 20 718 photons MeV^{-1} and a low detection limit of 0.31 μGy_{air} s^{-1}, enabling high-resolution imaging. In contrast, the 1D material consists of corner-sharing inorganic chains. It shows green emission from organic free excitons and poor scintillation performance. This study establishes that pyridinium cation engineering is a potent and promising strategy for the design and optimization of metal halide-based emitters and scintillators.

Received 27th October 2025
Accepted 3rd December 2025

DOI: 10.1039/d5sc08289g

rsc.li/chemical-science

Introduction

Scintillators are critical energy transducers that convert high-energy photons like X- or γ-rays into detectable visible light, underpinning technological progress in medical radiography, security screening, and high-energy physics research.[1–6] Commercial inorganic scintillators such as NaI:Tl, CsI:Tl, LYSO (Lu_2SiO_5:Ce), and BGO ($Bi_4Ge_3O_{12}$) exhibit high light yields but suffer from some intrinsic limitations.[7] For instance, LYSO requires energy-intensive synthesis,[8] while CsI:Tl degrades under ambient humidity, compromising their long-term stability.[9] Organic scintillators, though solution-processable, face low X-ray absorption coefficients and exciton utilization efficiency, restricting their practical utility.[10–12] Organic–inorganic hybrid metal halides (OIMHs), which leverage synergistic coordination between metal ions and organic ligands, have emerged as promising X-ray scintillators due to their solution processability, structural tunability, and exceptional optoelectronic properties.[13–15] Among them, lead-based OIHMs have been demonstrated to exhibit high X-ray absorption, a property arising from their heavy elements (Pb, Br/I). Nonetheless, their inherent toxicity and moisture instability impede practical deployment.[16,17] Although copper (Cu^+) and manganese (Mn^{2+}) alternatives mitigate lead's toxicity concerns, both face some fundamental limitations. Mn^{2+} emission suffers from spin-forbidden d–d transitions, leading to millisecond-scale lifetimes and narrow spectral tunability (510–650 nm).[18,19] Meanwhile, Cu^+ aggregates induce localized exciton emission confined to 440–580 nm, which also restricts performance optimization.[20] Consequently, there is an urgent and critical need for environmentally robust, high-performance alternatives that feature both scalable fabrication and superior, tunable optoelectronic properties.

Recently, antimony-based OIMHs (Sb-OIMHs) have emerged as a promising candidate for high-performance X-ray scintillator. Sb^{3+}'s stereochemical active $5s^2$ lone pair promotes strong electron-phonon coupling and facilitates self-trapped exciton (STE) formation—a mechanism enabling near-unity photoluminescence quantum yields (PLQYs) and broadband emissions.[21–23] Low-dimensional architectures, particularly 0D systems, further exploit quantum confinement to minimize self-absorption losses through large Stokes shifts.[24] Most currently reported Sb-OIMHs are based on phosphonium or alkylammonium cations.[25–27] For instance, the 0D compound

[a]*Key Laboratory of Photochemistry, Beijing National Laboratory for Molecular Sciences, CAS Research/Education Center for Excellence in Molecular Sciences, Institute of Chemistry, Chinese Academy of Science, Beijing 100190, China. E-mail: lizhongqiu@iccas.ac.cn; zhongyuwu@fzu.edu.cn*

[b]*School of Chemical Sciences, University of Chinese Academy of Sciences, Beijing 100049, China*

[c]*Institute of Molecular Engineering Plus, College of Chemistry, Fuzhou University, Fuzhou 350116, P. R. China. E-mail: jiabinchen@fzu.edu.cn*

[d]*College of Materials Science and Engineering, Fuzhou University, Fuzhou 350116, P. R. China. E-mail: qingliao@fzu.edu.cn*

$(C_{19}H_{18}P)_2Sb_2Cl_8$, built from triphenylmethylphosphonium cations and $[Sb_2Cl_8]^{2-}$ dimer units, exhibits efficient STE emission with a near-unity PLQY (Fig. 1a).[28] This material shows outstanding scintillator performance with a high light yield of 41 300 photons MeV^{-1} and a low detection limit of 45.6 nGy_{air} s^{-1}. The tetrapropylammonium-based 0D material $(C_{12}H_{28}N)_2SbCl_5$, consisting of isolated $[SbCl_5]^{2-}$ anions, achieves a high PLQY of 96.8%.[29] Nevertheless, despite observed radioluminescence (RL) under β-ray excitation, detailed studies on the scintillation properties and X-ray imaging capabilities of ammonium-cation-based antimony halides are scarce. The limited structural diversity offered by these conventional organic moieties restricts systematic tuning of the connectivity of $[SbX_n]$ polyhedra and associated exciton dynamics. Moreover, the role of organic components in modulating the emission mechanism (STE *vs.* free exciton, FE) and their impact on X-ray scintillation performance are still unclear, hindering the rational design of the next-generation Sb-OIMH scintillators.

To address these limitations, we demonstrate here the use of pyridinium cation as a superior alternative to conventional phosphonium or alkylammonium cations for simultaneously regulating the structural dimensionality and exciton behavior of Sb-OIMHs to achieve high-performance X-ray scintillation. Pyridinium derivatives are widely available and possess a great degree of structural tunability. The use of pyridinium derivatives as the organic cations of Sb-OIMHs enable a precise structure and dimensionality control through directional N^+–H···X hydrogen bonding and Coulombic interactions,[30–33] yielding either isolated $[SbX_n]$ polyhedra or linked chains. This in turn governs the exciton behavior and emission properties of the resulting materials. In this context, we found that the reaction of two structurally related pyridine derivatives, *N*-(pyridin-4-yl)benzamide (PBA) and 4-((*E*)-2-phenylvinyl)pyridine (PVP) in the presence of HCl, with $SbCl_3$ yielded 0D $(PBAH^+)_2SbCl_5$ and 1D $(PVPH^+)SbCl_4$ OIMHs, respectively (Fig. 1b). The 0D architecture of $(PBAH^+)_2SbCl_5$ promotes intense electron-phonon coupling and efficient STE formation, leading to superior broadband orange-red emission at 630 nm with a large Stokes shift of 262 nm and a near-unity PLQY. In particular, this STE-dominated mechanism delivers exceptional X-ray scintillation performance, achieving a high light yield of 20 718 photons MeV^{-1} and a low detection limit of 0.31 μGy_{air} s^{-1}. In contrast, 1D $(PVPH^+)SbCl_4$ shows organic exciton-dominated FE emission and exhibits poor scintillation performance. This work not only provides fundamental insights into how organic cations dictate the structural dimensionality and exciton dynamics of Sb-OIMHs, but also pioneers a pyridinium cation engineering strategy for the development of the next-generation radiation detection materials.

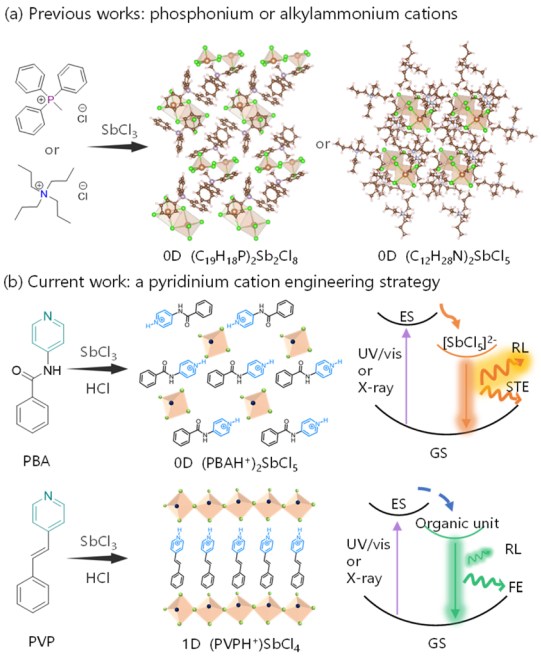

Fig. 1 (a) Previously reported 0D Sb-OIMHs based on phosphonium or alkylammonium cations. (b) Schematic illustration of the dimensionality control by a pyridinium cation engineering strategy to obtain 0D or 1D Sb-OIMHs with different exciton and RL properties. GS = ground state. ES = excited state.

Results and discussion

Structural dimensionality control

The single crystals of $(PBAH^+)_2SbCl_5$ and $(PVPH^+)SbCl_4$ were synthesized *via* a one-pot reaction procedure using PBA or PVP, $SbCl_3$ and HCl as the starting materials (Fig. 2a; see details in the Experimental section). The experimental power X-ray diffraction (PXRD) patterns of both materials are in good agreement with the simulated patterns derived from the single-crystal X-ray diffraction (SCXRD) data (Fig. 2b and c), confirming the high phase purity and uniformity of the as-synthesized crystals.

SCXRD analyses reveal that $(PBAH^+)_2SbCl_5$ crystallizes in the triclinic space group $P\bar{1}$, featuring isolated $[SbCl_5]^{2-}$ square pyramids with Sb–Cl bond lengths in the range of 2.38–2.77 Å (Fig. S1a). A network of N–H···Cl and C=O···H hydrogen bonds from the protonated pyridinium cation PBA^+ (pyridinium N–H···Cl: 2.65–2.77 Å; amide N–H···Cl: 2.76 Å; amide C=O···H: 2.47 Å) creates a 0D confinement, which spatially isolates $[SbCl_5]^{2-}$ polyhedra and yields extended Sb···Sb distances of 6.91–12.82 Å (Fig. 2d–f). The steric and electronic effects of the benzamide group work synergistically with this hydrogen-bonding network to stabilize the overall structure. In contrast, $(PVPH^+)SbCl_4$ adopts a monoclinic $P2_1/c$ structure. The corner-sharing $[SbCl_4]^-$ polyhedra form 1D zigzag chains along the *c*-axis (Sb–Cl: 2.39–2.97 Å; Fig. S1b), with a shortest intrachain Sb···Sb distances of 4.40 Å (Fig. 2g–i). The $PVPH^+$ cations stabilize the 1D framework *via* N–H···Cl hydrogen bonds (2.55 Å). As discussed below, the structural differences of these two materials lead to distinct emission and radioluminescence properties. In particular, the extended Sb···Sb separation (>6.9 Å) in 0D systems enables unconstrained lattice distortion, while 1D chains enforce rigid polyhedral connectivity that suppresses structural flexibility.

The chemical states of the constituent elements of $(PBAH^+)_2SbCl_5$ and $(PVPH^+)SbCl_4$ were further verified by X-ray

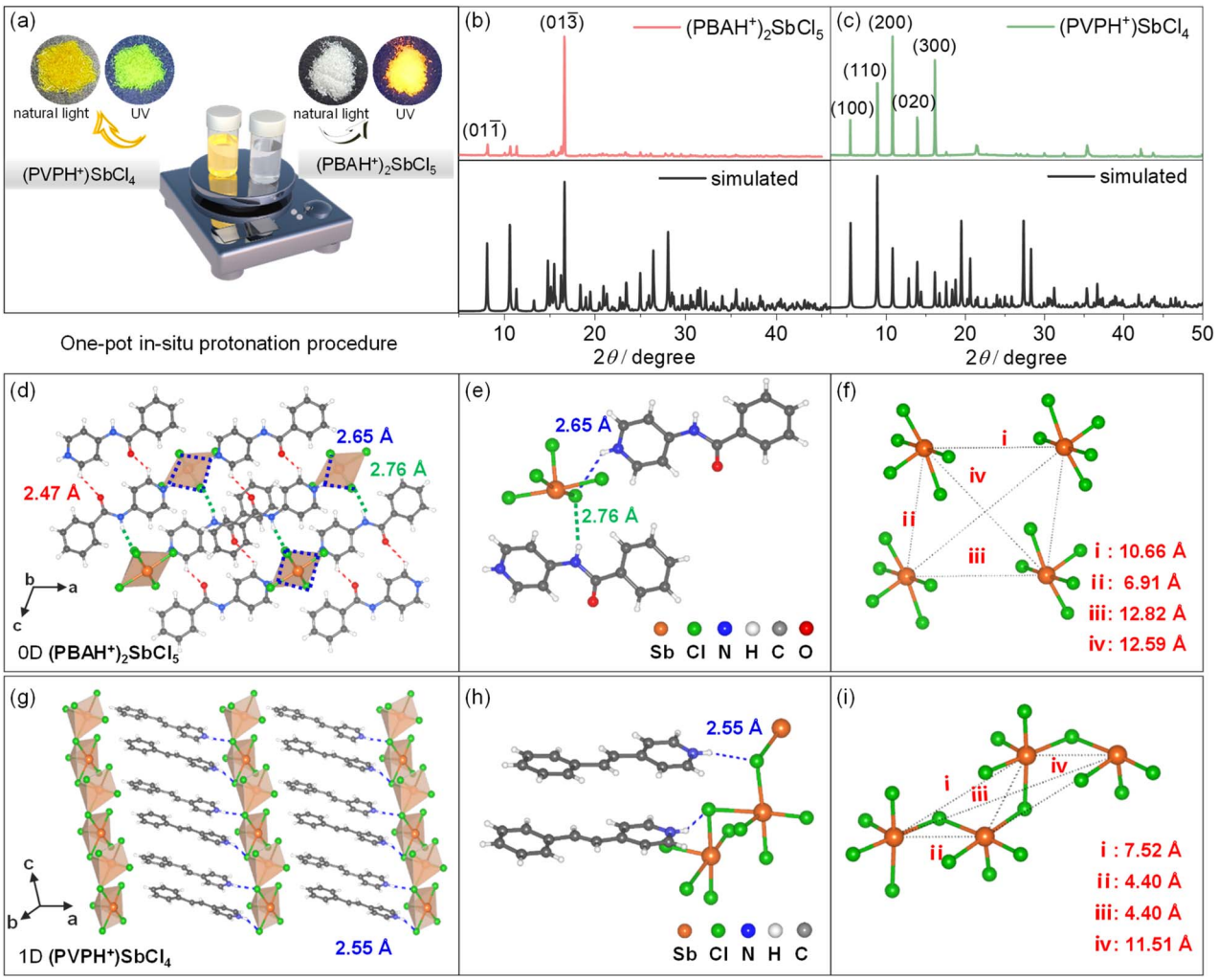

Fig. 2 (a) Schematic of the preparations of $(PBAH^+)_2SbCl_5$ and $(PVPH^+)SbCl_4$ crystals. Inset: photographs of crystals under ambient light and UV irradiation. (b) and (c) Experimental and simulated PXRD patterns of (b) $(PBAH^+)_2SbCl_5$ and (c) $(PVPH^+)SbCl_4$ crystals. (d)–(i) Single-crystal X-ray structures of (d)–(f) $(PBAH^+)_2SbCl_5$ and (g)–(i) $(PVPH^+)SbCl_4$. (e) and (h) Images showing the hydrogen-bonding networks between organic cations and inorganic units. (f) and (i) Images showing the Sb···Sb distances among adjacent inorganic units.

photoelectron spectroscopy (XPS) studies (Fig. S2). Furthermore, these materials demonstrate good thermal and environmental stability. Thermogravimetric analysis (TGA) indicates negligible weight loss for both compounds below 200 °C (Fig. S3). Additionally, their PXRD patterns remain unchanged after six months of exposure to ambient atmospheric conditions (Fig. S4).

Exciton dynamics

Scanning electron microscopy (SEM) shows that $(PBAH^+)_2SbCl_5$ forms as isolated rhombic blocks with widths of 50–80 μm (Fig. 3a), while $(PVPH^+)SbCl_4$ grows as elongated rods with lengths of a few hundreds of μm and widths of 15–25 μm (Fig. 3b). Under UV excitation, the 0D $(PBAH^+)_2SbCl_5$ crystals emit intense orange-red light, whereas the 1D $(PVPH^+)SbCl_4$ crystals show green emission. This dichotomy is consistent with their different bandgap energies (3.10 and 2.58 eV), respectively; Fig. S5.

The 0D $(PBAH^+)_2SbCl_5$ crystals exhibit hallmark signatures of STE emission with a broad and featureless photoluminescence (PL) band centered at 630 nm with a substantial Stokes shift of 262 nm and full width at half maxima (FWHM) of 135 nm (Fig. 3d). This emission possesses a microsecond-scale lifetime (τ = 4.42 μs, Fig. 3c) and a near-unity PLQY (>99%; Fig. S6). Photoluminescence excitation (PLE) spectral analysis suggests that STE-dominated emission is the exclusive radiative pathway of $(PBAH^+)_2SbCl_5$ (Fig. S7). The 0D structure with a geometric isolation of the inorganic units gives rise to a quantum-confined environment that intensifies electron-phonon coupling and thereby enables efficient STE formation.[34,35] The strength of this coupling is evidenced by a high Huang–Rhys factor (S = 12.45, see below). This coupling triggers significant Jahn–Teller distortion upon photoexcitation. The resultant lattice deformation creates localized potential wells that trap excitons, facilitating efficient triplet-to-singlet radiative recombination ($^3P_1 \rightarrow {}^1S_0$) at Sb^{3+} centers.[36] The broadband spectrum, large Stokes shift, and microsecond-scale lifetime of the STE-

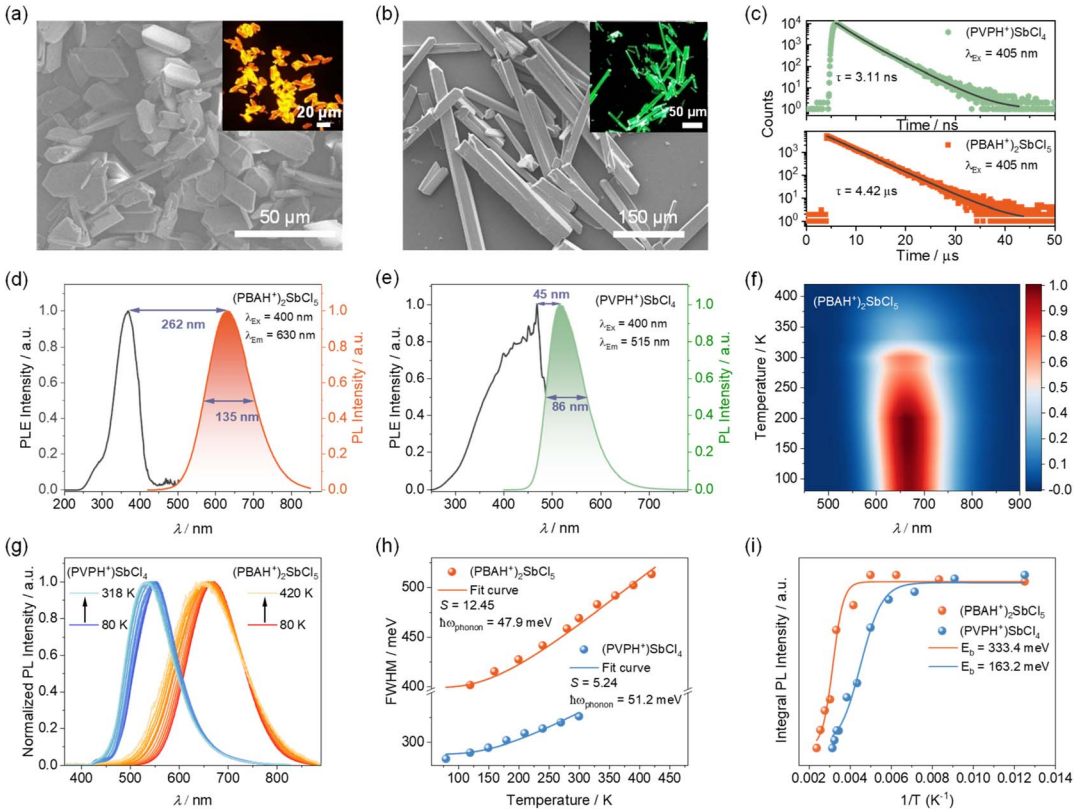

Fig. 3 (a) and (b) SEM images of (a) $(PBAH^+)_2SbCl_5$ and (b) $(PVPH^+)SbCl_4$. Inset: corresponding fluorescence microscopy images under UV excitation. (c) Time-resolved PL decay profiles of two crystals. (d) and (e) PLE and PL spectra of (d) $(PBAH^+)_2SbCl_5$ and (e) $(PVPH^+)SbCl_4$. (f) Temperature-dependent emission contour maps of $(PBAH^+)_2SbCl_5$. (g) Normalized temperature-dependent PL spectra of two crystals. (h) Plots of FWHM *versus* temperature. (i) Plots of PL intensity *versus* reciprocal temperature.

dominated emission offers distinct advantages over other processes like phosphorescence or thermally delayed fluorescence. These properties are particularly beneficial for X-ray scintillation, as they effectively suppress self-absorption losses and enable efficient photon integration with minimal afterglow, which is crucial for achieving high-resolution imaging and low-dose detection.

In contrast, the 1D $(PVPH^+)SbCl_4$ system displays fundamentally distinct exciton dynamics. It shows narrow green emission at 515 nm with FWHM of 86 nm, nanosecond lifetime

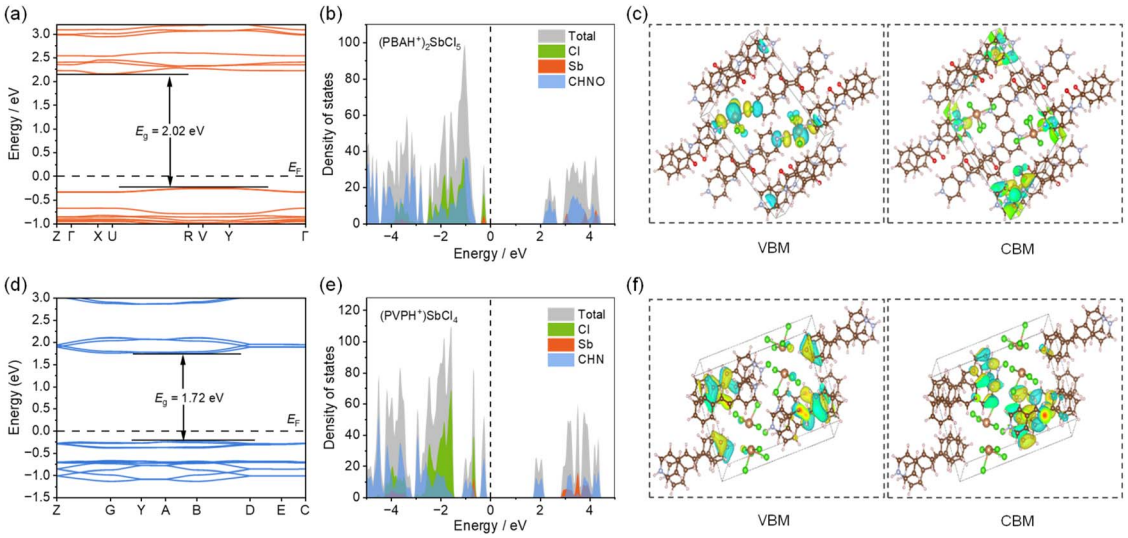

Fig. 4 (a) and (d) Calculated band structures, (b) and (e) density of states (DOS), and (c) and (f) electron density distributions of VBM and CBM of (a)–(c) $(PBAH^+)_2SbCl_5$ and (d)–(f) $(PVPH^+)SbCl_4$.

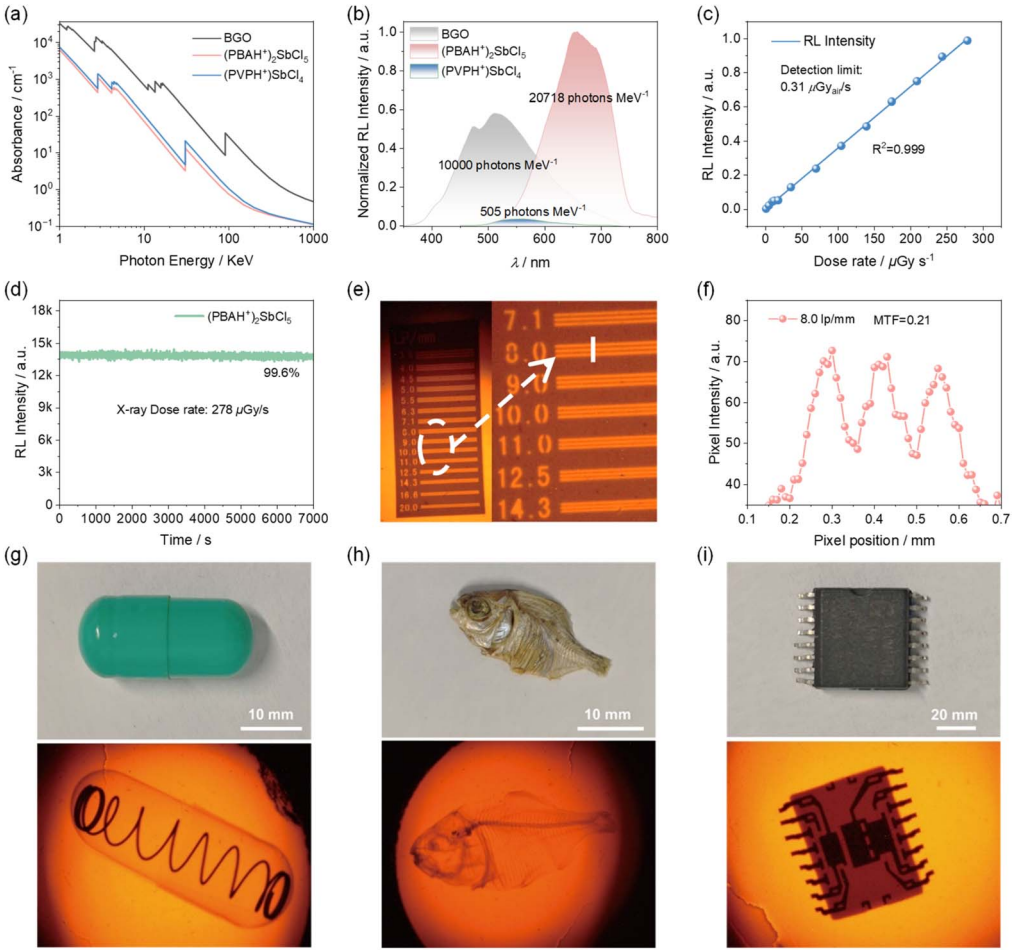

Fig. 5 (a) X-ray attenuation coefficient diagram of $(PBAH^+)_2SbCl_5$, $(PVPH^+)SbCl_4$ and BGO (from the NIST XCOM database). (b) RL spectra measured under X-ray irradiation (50 kV, 79 μA, dose rate = 278 $\mu Gy_{air}\ s^{-1}$). (c) The functional correlation between RL intensity and dose rate (0.7–278 $\mu Gy_{air}\ s^{-1}$) of X-ray for $(PBAH^+)_2SbCl_5$. (d) Radiation resistance test of $(PBAH^+)_2SbCl_5$ under prolonged X-ray exposure (278 $\mu Gy_{air}\ s^{-1}$ for 7000 s). (e) X-ray images of the line-pair card (type 25N: 3.5–20 lp per mm) and (f) corresponding pixel intensity profile across pixel positions (resolution: 8.0 lp per mm, MTF = 0.21 ± 0.01) under X-ray exposure. (g)–(i) Photographs captured under white light and X-ray illumination with $(PBAH^+)_2SbCl_5$ of (g) a capsule with a metallic, (h) a dried fish, (i) a printed circuit board.

of 3.11 ns (Fig. 3c), minimal Stokes shift of 45 nm (Fig. 3e), and moderate PLQY of 27.4% (Fig. S8). These characteristics unequivocally excludes STE emission.[37,38] The PL and PLE spectral profiles are independent of the excitation and emission conditions (Fig. S9), suggesting a single emission center. Control experiments show that the PVP·HCl organic salt has similar photophysics with emission maximum (λ_{em}) at 463 nm, PLQY of 31.77%, lifetime of 7.33 ns, and FWHM of 83 nm (Fig. S10 and S11). This suggests that the emission of $(PVPH^+)SbCl_4$ is very likely of the organic origin. The emission redshift of $(PVPH^+)SbCl_4$ *versus* PVP·HCl is caused by the influence of the inorganic units. The compressed 1D geometry induces strong lone-pair repulsion among adjacent Sb^{3+} centers, quenching Sb-centered emission and funneling excitonic energy to organic cations ($PVPH^+$).[39] The key photophysical parameters of both materials are summarized in Table S6, and their emissions are plotted using the Commission Internationale de l'Eclairage (CIE) chromaticity coordinates in Fig. S12. After storing for six months under ambient conditions, the PLQY values decrease from near-unity to 74.75% for $(PBAH^+)2SbCl_5$ and from 27.4% to 9.84% for $(PVPH^+)SbCl_4$, respectively; while their emission profiles remain essentially unchanged (Fig. S13 and S14). The PLQY reduction is likely initiated by surface hydrolysis due to the hygroscopic pyridinium cations, leading to the generation of non-radiative surface defects. The unchanged emission spectra suggest that this is a surface-dominated process, while the bulk emission centers remain stable.

To elucidate the exciton–phonon interaction mechanism, temperature-dependent PL spectra of the above two crystals have been investigated (Fig. 3f–i and S15). Both compounds exhibit a continuous blue-shift of their emission bands upon heating ($\Delta\lambda \approx$ 10–15 nm from 80–300 K, Fig. 3g), accompanied by progressive peak broadening. This phenomenon arises from two competing effects: thermally-induced lattice expansion, which reduces crystal field splitting, and enhanced electron-phonon coupling, which promotes exciton delocalization. Both are characteristic behaviors in Sb^{3+}-based halides.[40]

Concurrently, the emission intensities decrease exponentially with temperature due to the thermal activation of non-radiative pathways (Fig. S15). The observed linewidth broadening reflects a strengthening of exciton–lattice interactions.

Quantitative assessment of the electron-phonon coupling strength is achieved through the Huang–Rhys factor (S) analysis using the temperature-dependent FWHM evolution modeled by eqn (1):

$$\mathrm{FWHM} = 2.36\ \sqrt{S}\hbar\omega\sqrt{\coth\frac{\hbar\omega}{2k_{\mathrm{B}}T}} \quad (1)$$

where $\hbar\omega$ and k_{B} represent the energy of photon and the Boltzmann constant, respectively, and T stands for the temperature. Analysis of the spectra reveals that $(PBAH^{+})_2SbCl_5$ and $(PVPH^{+})SbCl_4$ have drastically distinct S value of 12.45 and 5.24, respectively (Fig. 3h). The extremely high S factor (>10) in the 0D system signifies profound lattice anharmonicity, enabling deep self-trapping potential wells essential for stable STE formation.[34,41] In contrast, the moderate electron-phonon coupling in the 1D compound stems from the geometrically constrained $[SbCl_4]^{-}$ polyhedra, where shortened Sb⋯Sb distances (4.40 Å) restrict distortion freedom and weaken lattice relaxation.[42,43]

The exciton binding energies (E_{b}) are further extracted from the Arrhenius analysis of integrated PL intensity by eqn (2):

$$I(T) = \frac{I_0}{1 + A\mathrm{e}^{-\frac{E_{\mathrm{b}}}{k_{\mathrm{B}}T}}} \quad (2)$$

with I_0 denote the theoretical 0 K intensity and A is the non-radiative attempt frequency. The 0D system exhibits a high E_{b} of 333.4 ± 8 meV, exceeding room-temperature thermal energy (26 meV) by >12-fold. In contrast, the 1D analogue shows reduced stability with a lower E_{b} of 163.2 ± 5 meV (Fig. 3i). This difference directly correlates with their structural dimensionality. The quantum-confined 0D environment localizes excitons through vigorous lattice distortion, which is further manifested by high S. This effect creates deep potential barriers to prevent thermal dissociation.[44] In contrast, the extended 1D chain structure permits exciton delocalization, lowering the binding energy barrier. Crucially, the ultrahigh E_{b} of $(PBAH^{+})_2SbCl_5$ underpins its exceptional radiation hardness and STE retention efficiency under ionizing radiation.

Theoretical calculations

Density functional theory (DFT) calculations provide fundamental insights into the electronic origins of the contrasting emission mechanisms between 0D and 1D architectures. Band structure analysis reveals that $(PBAH^{+})_2SbCl_5$ adopts an indirect bandgap with a bandgap energy E_{g} of 2.02 eV (Fig. 4a), whereas $(PVPH^{+})SbCl_4$ exhibits a direct bandgap with E_{g} of 1.72 eV (Fig. 4d). While these values underestimate experimental optical gaps (3.10 eV *vs.* 2.58 eV),[45,46] the relative trend aligns with the spectroscopic measurements. Crucially, the projected density of states (PDOS) unravels the atomic-scale dichotomy. In 0D $(PBAH^{+})_2SbCl_5$, the valence band maximum (VBM) arises from the hybridization of Sb 5s/5p and Cl 3p orbital, while the conduction band minimum (CBM) is dominated by the π* orbitals of PBA^{+} cations (Fig. 4b). This inorganic VBM and organic CBM character creates a hybrid charge-transfer state that localizes excitons on the $[SbCl_5]^{2-}$ clusters prior to the recombination through organic manifolds, directly enabling STE formation.[47] This theoretical model is corroborated by the UV-vis absorption data (Fig. S16), which shows a distinct low-energy shoulder band at 360–420 nm. This feature is attributed to a charge-transfer transition between the inorganic $[SbCl_5]^{2-}$ clusters and the organic $PBAH^{+}$ cations, as it cannot be assigned to the intrinsic transitions of either isolated component. In contrast, in 1D $(PVPH^{+})SbCl_4$, both VBM and CBM originate from the π and π* orbitals of PVP^{+} (C 2p/N 2p, Fig. 4e), signifying purely organic excitons confined within the cation framework.[48] This dimensional divergence is further visualized in the charge density difference maps (Fig. 4c and f). The excitation of 0D system triggers pronounced electron density redistribution from Sb–Cl bonds to pyridinium group, leading to exciton localization across inorganic–organic interfaces. In contrast, the excitation of 1D analogue displays intramolecular polarization within the PVP^{+} moiety, consistent with the localized π → π* transitions.

X-ray scintillation and imaging

Theoretical X-ray attenuation analysis reveals that both Sb-OIMHs exhibit reduced absorption coefficients relative to the inorganic scintillator BGO across photon energies of 1–1000 keV using the XCOM web database, consistent with their lower crystalline densities (Fig. 5a).[49] Under X-ray excitation, both materials exhibit RL spectra very similar to their PL profiles, confirming the preservation of the same emission centers and recombination pathways regardless of the excitation source (Fig. 5b). The slight redshift (∼5 nm) of the observed RL *versus* corresponding PL spectra of both samples likely originates from the instrumental calibration factors. The relative light yield of $(PBAH^{+})_2SbCl_5$ was calculated to be 20 718 photons MeV^{-1} according to the commercial BGO scintillator as a reference. This performance is 41-fold higher than the 1D $(PVPH^{+})SbCl_4$ counterpart (505 photons MeV^{-1}; Fig. 5b and S17). The excellent RL performance of the 0D $(PBAH^{+})_2SbCl_5$ originates from the synergistic advantages of STE emission including the near-unity radiative efficiency, a high exciton binding energy that suppresses thermal quenching, and a large Stokes shift that eliminate self-reabsorption.[50] In contrast, the organic exciton emission of the 1D $(PVPH^{+})SbCl_4$ suffers from competitive non-radiative decay and inherent self-absorption, fundamentally limiting its scintillation output.

Further evaluation establishes that $(PBAH^{+})_2SbCl_5$ is a premier low-dose detection platform. It exhibits an outstanding dose linearity across the clinically relevant ranges of 0.7–278 $\mu Gy_{air}\ s^{-1}$ (Fig. 5c, S18 and Table S7), with a rather low detection limit of 0.31 $\mu Gy_{air}\ s^{-1}$ at a signal-to-noise ratio (SNR) of 3. This represents 94% reduction *versus* the standard medical diagnostics (5.5 $\mu Gy_{air}\ s^{-1}$).[51] Radiation hardness tests confirm the material's exceptional stability, showing <1% signal attenuation after prolonged exposure for 7000 s at 278 $\mu Gy_{air}\ s^{-1}$

and negligible degradation through 20 operational cycles (1200 s total duration; Fig. 5d and S19). These metrics surpass most conventional scintillators in both sensitivity and operational stability, attributed to the material's robust STE potential wells and high crystallinity. Critically, a comparative analysis (Table S8) demonstrates that this 0D $(PBAH^+)_2SbCl_5$ exhibits comparable or even superior overall scintillation performance to other reported Sb-based OIHMs, making it a valuable alternative candidate for scintillation applications.

The translation of the superior scintillation properties of $(PBAH^+)_2SbCl_5$ into practical applications has been demonstrated through X-ray imaging studies (Fig. S20). The solution-processed scintillator screens, fabricated *via* 24 hours ball milling of $(PBAH^+)_2SbCl_5$ crystals in dichloromethane followed by vacuum filtration, achieves a remarkable spatial resolution of 8.0 lp per mm (MTF = 0.21) as quantified through standardized line-pair tests (Fig. 5e and f).[52–54] This excellent X-ray imaging performance enables clear visualization of sub-millimeter mechanical features in encapsulated spring assemblies, trabecular bone microarchitecture in biological specimens, and micron-scale circuit traces in multilayer PCBs (Fig. 5g–i). The high contrast resolution and low noise characteristics observed across these diverse imaging targets confirm the material's versatility for both medical radiography and industrial inspection applications.

Conclusions

In summary, we demonstrate a pyridinium cation engineering method to control the structural dimensionality and exciton behavior of Sb-OIMH scintillators. By introducing an amide linker as an additional hydrogen-bonding site, a 0D Sb-OIMH with isolated $[SbCl_5]^{2-}$ polyhedra has been obtained, which exhibit strong electron-phonon coupling and efficient STE emission. This scintillator is characterized with a high light yield and low detection limit, making it suitable for high-resolution X-ray imaging. In contrast, a 1D Sb-OIMH with compressed Sb···Sb distances has been obtained with 4-((*E*)-2-phenylvinyl)pyridine, which favors the emission of organic free excitons but exhibits poor scintillation. This work establishes that a delicate change of the pyridinium cation may have a significant impact on the dimensionality, exciton property, and scintillation performance of the resulting OIMH. Pyridinium cation engineering is believed to become a promising strategy for designing and optimizing of metal halide emitters and scintillators. Our ongoing research efforts focus on the application of this pyridinium cation engineering strategy to other lead-free metal halide systems. We anticipate this approach will enable the rational design of metal halides with tailored optoelectronic properties.

Author contributions

Conceptualization: Y.-W. Zhong, Z.-Q. Li, and J. Yao. Methodology: Y.-W. Zhong, Z.-Q. Li, Q. Liao, and J. Chen. Investigation: Y.-Y. Zhao, L. Zhang, Q. Liao, and J. Chen. Visualization: Y.-Y. Zhao, Z.-Q. Li, Y.-W. Zhong, and J.-C. Chen. Funding acquisition: Z.-Q. Li, Q. Liao, and Y.-W. Zhong. Project administration: Z.-Q. Li, Y.-W. Zhong, Q. Liao and J. Chen. Supervision: Y.-W. Zhong, J. Yao, and M. Lin. Writing – original draft: Y.-Y. Zhao. Writing – review & editing: Y.-W. Zhong, Z.-Q. Li, and Q. Liao.

Conflicts of interest

There are no conflicts to declare.

Data availability

The data supporting this article have been included as part of the supplementary information (SI). Supplementary information: details of experimental methods, characterisation data. See DOI: https://doi.org/10.1039/d5sc08289g.

CCDC 2363201 and 2431220 contain the supplementary crystallographic data for this paper.[55a,b]

Acknowledgements

This work was financially supported by the National Natural Science Foundation of China (grants 22305251 and 52303222) and National Key R&D Program of China (2022YFA1204401 and 2023YFE0125200). Z.-Q. L. acknowledges the support of Beijing Molecular Science (BMS) Junior Fellow of BNLMS.

Notes and references

1 W. Ma, Y. Su, Q. Zhang, C. Deng, L. Pasquali, W. Zhu, Y. Tian, P. Ran, Z. Chen, G. Yang, G. Liang, T. Liu, H. Zhu, P. Huang, H. Zhong, K. Wang, S. Peng, J. Xia, H. Liu, X. Liu and Y. M. Yang, *Nat. Mater.*, 2021, **21**, 210–216.
2 J.-X. Wang, L. Gutiérrez-Arzaluz, X. Wang, T. He, Y. Zhang, M. Eddaoudi, O. M. Bakr and O. F. Mohammed, *Nat. Photonics*, 2022, **16**, 869–875.
3 J. Fan, H. Li, W. Liu and G. Ouyang, *Angew. Chem., Int. Ed.*, 2025, **64**, e202425661.
4 Y. Chen, S. Niu, Y. Li, W. Dou, X. Yang, C. Shan and G. Shen, *Adv. Mater.*, 2024, **36**, 2404656.
5 X. Yan, S.-Y. Song, S. Liang, K.-K. Liu, X.-T. Liu and C. Lu, *Chem. Sci.*, 2025, **16**, 16770–16779.
6 H. Chen, X. Yang, Y. Ye, H. Hong, Q. Wei, Y. Zhu and M. J. Lin, *Angew. Chem., Int. Ed.*, 2025, **64**, e202506118.
7 P. Singh, G. Dosovitskiy and Y. Bekenstein, *ACS Nano*, 2024, **18**, 14029–14049.
8 L. Fan, Y. Wu, Z. Zhang, Y. Shi and J. Xie, *Opt. Mater.*, 2020, **99**, 109563.
9 Z. Wang, R. T. Williams, J. Q. Grim, F. Gao and S. Kerisit, *Phys. Status Solidi B*, 2013, **250**, 1532–1540.
10 X. Wang, H. Shi, H. Ma, W. Ye, L. Song, J. Zan, X. Yao, X. Ou, G. Yang, Z. Zhao, M. Singh, C. Lin, H. Wang, W. Jia, Q. Wang, J. Zhi, C. Dong, X. Jiang, Y. Tang, X. Xie, Y. Yang, J. Wang, Q. Chen, Y. Wang, H. Yang, G. Zhang, Z. An, X. Liu and W. Huang, *Nat. Photonics*, 2021, **15**, 187–192.
11 Y.-H. Chen, G.-Z. Zhang, F.-H. Chen, S.-Q. Zhang, X. Fang, H.-M. Chen and M.-J. Lin, *Chem. Sci.*, 2024, **15**, 7659–7666.

12 Y. Zhang, M. Chen, X. Wang, M. Lin, H. Wang, W. Li, F. Chen, Q. Liao, H. Chen, Q. Chen, M. Lin and H. Yang, *CCS Chem.*, 2024, **6**, 334–341.
13 W. Wei, Y. Zhang, Q. Xu, H. Wei, Y. Fang, Q. Wang, Y. Deng, T. Li, A. Gruverman, L. Cao and J. Huang, *Nat. Photonics*, 2017, **11**, 315–321.
14 J.-H. Chen, J.-B. Luo, Z.-L. He, Q.-P. Peng, J.-H. Wei, Z.-Z. Zhang, X.-X. Guo and D.-B. Kuang, *Chem. Sci.*, 2025, **16**, 9375–9384.
15 Q. Zhou, W. Li, J. Xiao, A. Li and X. Han, *Adv. Funct. Mater.*, 2024, **34**, 2402902.
16 H. Wei, Y. Fang, P. Mulligan, W. Chuirazzi, H.-H. Fang, C. Wang, B. R. Ecker, Y. Gao, M. A. Loi, L. Cao and J. Huang, *Nat. Photonics*, 2016, **10**, 333–339.
17 A. Xie, F. Maddalena, M. E. Witkowski, M. Makowski, B. Mahler, W. Drozdowski, S. V. Springham, P. Coquet, C. Dujardin, M. D. Birowosuto and C. Dang, *Chem. Mater.*, 2020, **32**, 8530–8539.
18 C. Wang, Y. Li and Z. Deng, *Chem. Sci.*, 2025, **16**, 15796–15814.
19 J.-Y. Yao, Q.-R. Ding, H. Zeng, J.-Y. Wang, C.-M. Shi, L.-J. Xu and Z.-N. Chen, *Angew. Chem., Int. Ed.*, 2025, **64**, e202502099.
20 H. Zhang, B. Yu, Y. Tan, A. Ying, W. He, Z. Jia, Q. Lin and S. Gong, *Sci. China:Chem.*, 2025, **68**, 4245–4254.
21 W. Han, P. Cheng, J. Guan, Q. Li, Y. Wang, Z. Wang, T. Rasing, Y. Zheng, J. Xu and X. H. Bu, *Angew. Chem., Int. Ed.*, 2025, **64**, e202500786.
22 H. Liu, T. B. Shonde, F. Gonzalez, O. J. Olasupo, S. Lee, D. Luong, X. Lin, J. S. R. Vellore Winfred, E. Lochner, I. Fatima, K. Hanson and B. Ma, *Adv. Mater.*, 2023, **35**, 2209417.
23 D.-Y. Li, H.-Y. Kang, Y.-H. Liu, J. Zhang, C.-Y. Yue, D. Yan and X.-W. Lei, *Chem. Sci.*, 2024, **15**, 953–963.
24 T. Huang and B. Zou, *Nanomaterials*, 2023, **13**, 2867.
25 Z. Xu, N. Li, X. Yan, X. Wang, T. He, Z. Yang and S. Liu, *Adv. Opt. Mater.*, 2024, **12**, 2301477.
26 H. Huang, Y. Yang, S. Qiao, X. Wu, Z. Chen, Y. Chao, K. Yang, W. Guo, Z. Luo, X. Song, Q. Chen, C. Yang, Y. Yu and Z. Zou, *Adv. Funct. Mater.*, 2024, **34**, 2309112.
27 H. Chen, H. Cui, T. Jiang, Z. Feng, Y. Yan, S. Liu and Q. Zhao, *J. Mater. Chem. C*, 2024, **12**, 12325–12331.
28 H. Meng, Y. Li, F. Zhang, S. Niu, M. Zhu, Z. Shi and G. Shen, *Adv. Funct. Mater.*, 2025, **35**, 2412597.
29 L. Lian, P. Zhang, X. Zhang, Q. Ye, W. Qi, L. Zhao, J. Gao, D. Zhang and J. Zhang, *ACS Appl. Mater. Interfaces*, 2021, **13**, 58908–58915.
30 Z.-Q. Li, D.-X. Ma, F.-F. Xu, T.-X. Dan, Z.-L. Gong, J.-Y. Shao, Y.-S. Zhao, J. Yao and Y.-W. Zhong, *Angew. Chem., Int. Ed.*, 2022, **61**, e202205033.
31 Y.-Y. Zhao, Z.-Q. Li, J.-Y. Shao and Y.-W. Zhong, *Cryst. Growth Des.*, 2023, **23**, 9086–9093.
32 L. Gao, G. V. Baryshnikov, A. Ali, A. Kuklin, C. Qian, X. Zhang, F. Chen, T. Yi and H. Wu, *Angew. Chem., Int. Ed.*, 2024, **63**, e202318497.
33 S. Xiong, Y. Xiong, D. Wang, Y. Pan, K. Chen, Z. Zhao, D. Wang and B. Z. Tang, *Adv. Mater.*, 2023, **35**, 2301874.
34 J.-F. Liao, Z. Zhang, L. Zhou, Z. Tang and G. Xing, *Angew. Chem., Int. Ed.*, 2024, **63**, e202404100.
35 Z. Li, Y. Li, P. Liang, T. Zhou, L. Wang and R.-J. Xie, *Chem. Mater.*, 2019, **31**, 9363–9371.
36 K. M. McCall, V. Morad, B. M. Benin and M. V. Kovalenko, *ACS Mater. Lett.*, 2020, **2**, 1218–1232.
37 R. Chen, C. Sun, X. Cheng, Y. Lin, J. Zhou, J. Yin, B.-B. Cui and L. Mao, *Inorg. Chem.*, 2023, **62**, 9722–9731.
38 H. Peng, S. Yu, Q. Wei, L. Kong, Z. Du, J. Zhao and B. Zou, *Adv. Funct. Mater.*, 2024, **34**, 2411807.
39 C. Sun, Z. Deng, Z. Li, Z. Chen, X. Zhang, J. Chen, H. Lu, P. Canepa, R. Chen and L. Mao, *Angew. Chem., Int. Ed.*, 2023, **62**, e202216720.
40 D.-Y. Li, J.-H. Song, Z.-Y. Xu, Y.-J. Gao, X. Yin, Y.-H. Hou, L.-J. Feng, C.-Y. Yue, H. Fei and X.-W. Lei, *Chem. Mater.*, 2022, **34**, 6985–6995.
41 Z. Ma, X. Ji, S. Lin, X. Chen, D. Wu, X. Li, Y. Zhang, C. Shan, Z. Shi and X. Fang, *Adv. Mater.*, 2023, **35**, 2300731.
42 Y. Hui, S. Chen, R. Lin, W. Zheng and F. Huang, *Mater. Chem. Front.*, 2021, **5**, 7088–7107.
43 X. Han, P. Cheng, S. Han, Z. Wang, J. Guan, W. Han, R. Shi, S. Chen, Y. Zheng, J. Xu and X.-H. Bu, *Chem. Sci.*, 2024, **15**, 3530–3538.
44 C. Li, Z. Luo, Y. Liu, Y. Wei, X. He, Z. Chen, L. Zhang, Y. Chen, W. Wang, Y. Liu, X. Chang and Z. Quan, *Adv. Opt. Mater.*, 2022, **10**, 2102746.
45 D. Chen, S. Hao, G. Zhou, C. Deng, Q. Liu, S. Ma, C. Wolverton, J. Zhao and Z. Xia, *Inorg. Chem.*, 2019, **58**, 15602–15609.
46 Q. Mo, Q. Qian, Y. Shi, W. Cai, S. Zhao and Z. Zang, *Adv. Opt. Mater.*, 2022, **10**, 2201509.
47 H. Meng, B. Chen, W. Zhu, Z. Zhou, T. Jiang, X. Xu, S. Liu and Q. Zhao, *Laser Photonics Rev.*, 2023, **17**, 2201007.
48 B. Zhuang, Z. Jin, J. Deng, H. Xiong, W. Li and J. Fan, *Adv. Opt. Mater.*, 2023, **11**, 2300888.
49 S.-B. Xiao, X. Zhang, X. Mao, H.-J. Yang, Z.-N. Chen and L.-J. Xu, *Adv. Funct. Mater.*, 2024, **34**, 2404003.
50 J. Perego, C. X. Bezuidenhout, I. Villa, F. Cova, R. Crapanzano, I. Frank, F. Pagano, N. Kratochwill, E. Auffray, S. Bracco, A. Vedda, C. Dujardin, P. E. Sozzani, F. Meinardi, A. Comotti and A. Monguzzi, *Nat. Commun.*, 2022, **13**, 3504.
51 Q. Chen, J. Wu, X. Ou, B. Huang, J. Almutlaq, A. A. Zhumekenov, X. Guan, S. Han, L. Liang, Z. Yi, J. Li, X. Xie, Y. Wang, Y. Li, D. Fan, D. B. L. Teh, A. H. All, O. F. Mohammed, O. M. Bakr, T. Wu, M. Bettinelli, H. Yang, W. Huang and X. Liu, *Nature*, 2018, **561**, 88–93.
52 K. Masaoka, *Opt. Express*, 2019, **27**, 1345.
53 R. Gerst, Z. Cseresnyés and M. T. Figge, *Nat. Methods*, 2023, **20**, 168–169.
54 L.-J. Xu, X. Lin, Q. He, M. Worku and B. Ma, *Nat. Commun.*, 2020, **11**, 4329.
55 (*a*) CCDC 2363201: Experimental Crystal Structure Determination, 2025, DOI: 10.5517/ccdc.csd.cc2kb39b; (*b*) CCDC 2431220: Experimental Crystal Structure Determination, 2025, DOI: 10.5517/ccdc.csd.cc2mlwgl.